PROCESSING OF RARE EARTH METAL OXIDE FOR USE AS A MASTER ALLOY IN THE METALLURGICAL INDUSTRY

I. S. Nikulin,[1] **T. B. Nikulicheva,**[2] **N. V. Anosov,**[3] **M. N. Yapryntsev,**[4]
A. O. Vyugin,[5] **N. I. Alfimova,**[6] **and Yu. I. Karlina**[7]

UDC 669.1; 669.85

Consumption of rare-earth metal (REM) oxides, such as cerium and lanthanum, is significantly lower than their production. This discrepancy is attributed to the complex extraction of all REMs, where the share of cerium is approximately 40%. This article proposes a method for processing REM oxides for their use as master alloys in ferrous metallurgy products. REMs, in the form of modifiers for steels and alloys, are widely used. However, despite their wide usage, owing to the complexity of the REM production technology, they tend to have a high market value. This study explores the preparation of a cerium carbide (CeC_2) master alloy for the modification of steels and cast irons. The proposed method aims to reduce the cost of the alloying process and simultaneously increase the demand for REM oxides. Using a high-temperature synthesis process, CeC_2 was obtained for the modification of steel and cast iron. For this purpose, cerium dioxide (CeO_2), graphite (C), and ARMCO-iron (Fe) were mixed in a specific percentage ratio by weight: 5.4% C, 19.5% CeO_2, and 75.1% Fe. Following this, the reaction mixture was heated in a furnace to a temperature of 1650°C and held for 30 min, with a residual pressure in the furnace of 10^{-1} mbar. The synthesis was performed in the temperature range of 1300–1650°C, with the highest reaction rate of at a temperature of 1520°C. Both elemental and X-ray diffraction analyses indicated that CeO_2 was the end product of the synthesis process. The master alloy does not undergo hydrolysis because CeC_2 is synthesized in the liquid phase of iron. It has been established that the technology for producing a cerium carbide alloy involving high-temperature heating in a resistive furnace, enables the production of a material with reproducible properties.

Keywords: carbide, cerium, alloy, synthesis, steel, cast iron, ferrous metallurgy, rare-earth metals.

Introduction

The consumption and production of rare-earth elements and their compounds continues to grow, reflecting their increasing importance in a range of industries. The development of rare-earth metal (REM) production is becoming a critical task for the Russian economy is the development of rare-earth metal production. Although the consumption of these elements does not compare to that of the large-scale raw materials industries, even small amounts can yield products with unique properties and characteristics.

[1] Belgorod National Research University, Belgorod, Russia; e-mail: ivanikulin@yandex.ru.

[2] Belgorod National Research University, Belgorod, Russia; e-mail: t_nikulicheva@inbox.ru.

[3] Belgorod National Research University, Belgorod, Russia; e-mail: nikit.a1999@ya.ru.

[4] Belgorod National Research University, Belgorod, Russia; e-mail: yaprintsev@bsu.edu.ru.

[5] Belgorod National Research University, Belgorod, Russia; e-mail: alexeyvyugin@yandex.ru.

[6] Belgorod State Technological University named after V. G. Shukhov, Belgorod, Russia; e-mail: alfimovan@mail.ru.

[7] Moscow State University of Civil Engineering, Moscow, Russia; e-mail: jul.karlina@gmail.com.

(REMs comprise a group of 17 elements, including scandium, yttrium, lanthanum, and lanthanides (such as Ce and Lu).Certain REMs have a value that surpasses gold and platinum thanks to their unique applications. They are used in various fields such as aircraft manufacturing, medicine, superconducting materials, and electronic devices like phones and computers. REMs are integral to high-technology applications such as electronics, green technology, energy-saving incandescent light bulbs, and fighter jet engines towing to their unique chemical, electrical, magnetic, and luminescent properties [1].

REMs play a significant role in altering the structure and properties of steel and cast iron [5–18]. They are fully soluble in liquid iron, whereas in solid iron, their solubility is limited to just 0.2% slightly increasing to 0.35–0.4% at 600°C. Any excess REM content not associated with sulfur, oxygen, and phosphorus is expelled during steel solidification at the boundary of primary crystals. Given the large size of REM atoms, which prevents the formation of wide solubility areas in other metals in solid state [6], it is uncommon to add more than 0.2 wt.% in steel. However, even this minimal amount can significantly affect the structure and improve the properties of steels. In the industry, rare-earth elements are typically used in metallic form as additives to steels and alloys though their complex production technology determines their high market value.

One of the most commonly used REM additives for steels and cast irons is cerium (Ce). It forms stable oxides, sulfides, and oxysulfides. In liquid steel, these elements combine easily with oxygen and sulfur because of the low Gibbs energy of formation of their compounds [4]. Because the melting points of oxides, sulfides, and oxysulfidoids are quite high, they precipitate as solid insoluble particles in liquid steel.

Cerium and its compounds account for approximately 40% of the production volume of all REMs. The widespread use of REMs has led to a global demand of approximately 136,000 tons per year. Currently, there are approximately 100 million tons of REM oxide reserves worldwide, spread across more than 30 countries.

The main methods for obtaining individual rare-earth elements are the electrolysis of chlorides and fluorides. In the former case, the process involves working with elemental chlorine, which can be used advantageously as a reagent. Operating in fluoride oxide systems poses fewer safety challenges. However, a significant disadvantage is the high consumption of electrodes necessary for the production of anodic oxygen. In both scenarios, the main expense is the electricity required for electrolysis. It is worth noting that the usual energy consumption for auxiliary operations such as drying, calcination, and equipment operation is orders of magnitude less than that required for electrolysis. Regardless of the variant, maintaining productivity in electrolysis technology demands substantial infrastructure costs.

The reduction of anhydrous chlorides/fluorides with more active metals is less common owing to its relative ease of implementation. Calcium serves as the main reagent. The cost of metal reduction is a major expense, with the price of calcium being comparable to that of the resulting cerium. This raises questions about the effectiveness of independent development in this area. The limited profitability of such production is confirmed by the fact that calcium production plants often coincide with the production of rare-earth elements such as uranium. This arrangement allows for closed-cycle production for chlorine, thereby enhancing the overall efficiency of the calcium thermic process [2, 3].

When cerium is introduced into steel, it purifies the metal by eliminating harmful impurities such as sulfur, oxygen, and phosphorus. This process not only refines the steel but also alters the structure and characteristics of the secondary phases within it. In the industry, cerium is typically introduced into steel in the form of a ferrocerium alloy, in which cerium constitutes approximately 40% of the total composition. Owing to the complexity of the production process, the cost of the master alloy exceeds the combined costs of calcium and magnesium [5–12, 19–21].

The use of cerium carbide to alloy steel and cast iron could potentially reduce the associated costs. This would likely boost the wider application of this method in the field of metallurgy.

With this in mind, the objective of this study was to produce a master alloy containing cerium dicarbide (CeC_2) for the modification of steels and cast irons.

Materials and Methods

To produce cerium carbide, we used 99.5% pure cerium dioxide (CeO_2), carbon (C) in the form of graphite with a purity of 99.99%, and 99.92% pure ARMCO-iron (technically pure iron).

Cerium dioxide and graphite were homogeneously mixed in a weight ratio of 3.6:1. This ratio was derived from the stoichiometry of the reaction of Eq. (4). ARMCO-iron was then added to the cerium dioxide and graphite mixture in a ratio of 3:1. The resulting mixture was ground in a ball mill with acetone using stabilized zirconium spheres for 4 h. The powdered suspension was sieved using a 10 μm mesh to separate granules. Subsequently, the suspension was dried under vacuum for 2 h at 100°C. The dried mixture was then pressed into a mold with dimensions of $8 \times 8 \times 100$ mm, forming a rectangular parallelepiped. Each mold contained 3 g of the sample and was compressed under a load of 5 tones. The compressed samples were placed in an aluminum oxide crucible, which was then placed in a furnace.

The synthesis of CeC_2 took place in a Nabertherm GmbH vacuum furnace equipped with a high-precision electronic barometer. The process involved sintering cerium dioxide and carbon (graphite) to yield cerium dicarbide (CeC_2). Before use, the furnace was purged with high-purity argon, followed by the creation of a 10^{-1} mbar. The molded samples were heated to 1650°C, maintained at this temperature for 30 min, and then cooled together with the furnace to room temperature at a rate of 15°C/min. After cooling, the crucible containing the sintered sample was removed. To prevent hydrolysis, the prepared sample was placed in hexane (C_6H_{14}). The adoption of these optimal technological parameters was based on the results of prior studies.

For metallographic studies, mechanical processing was performed under "glove box" conditions. Before processing, the internal volume was cleaned with high-purity argon. Then, the sample was processed manually using Struers sandpaper with a grit size ranging from 500 to 2000, before being placed in hexane.

The obtained samples were analyzed using a Quanta 600 scanning electron microscope equipped with an EDAX X-ray microanalysis attachment. A 10^{-2} Pa vacuum was created in the working area. The elemental composition was determined using the EDAX APEX software.

The main method we used to determine the phase composition of the resulting sample was X-ray phase analysis. These studies were conducted on a high-resolution X-ray diffractometer smartLAB Rigaku. The sample was encased in Mylar film (an X-ray transparent material) to reduce exposure to air. For the X-ray diffraction analysis of the phase composition, we used Cu–Ka radiation (wavelength $\lambda = 0.154178$ nm) together with Soler slits. Using a θ–2θ scanning scheme with Bragg–Brentano focusing, we obtained the diffraction spectrum for phase analysis. This was performed in the angular range from 5 to 100 degrees 2θ. The survey was performed in "point-by-point" mode using a scanning step $\Delta(2\theta) = 0.02$ degrees at a rate of 2 degrees/min, with an operating voltage of 40 kV, and a current of 100 mA.

The PDXL RIGAKU software package was used to refine the profile of the experimental X-ray diffraction patterns. The background was subtracted using the Sonneveld–Visser method, the experimental profile was smoothed using the Savitsky–Golay method, and components ka1 and ka2 were separated using the Reichinger method. To describe the diffraction maxima, we used a combination of the Gaussian and Lorentz functions.

By approximating each reflection in the diffraction patterns of the studied samples with a pseudo-Voigt function, we could precisely determine the reflection positions. We considered the shift caused by the overlap of reflections at half maximum intensity and intensification. The phase composition was determined using the ICCD PDF-2 database (2008).
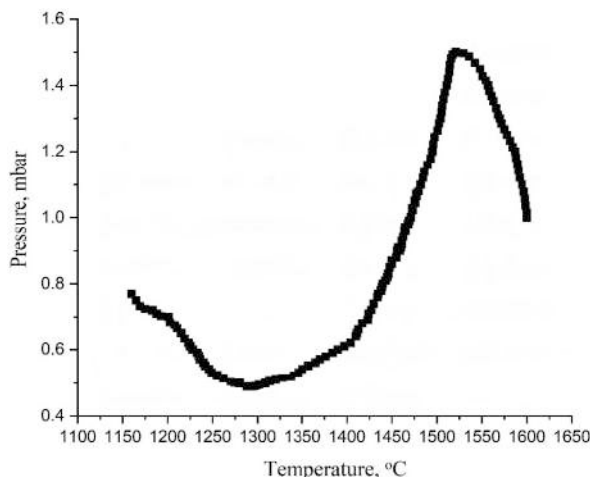
Fig. 1. Dependence of pressure on temperature in the furnace working area.

Results and Discussion

To determine the synthesis temperature of cerium dicarbide, we plotted a graph of pressure versus temperature inside the chamber (Fig. 1). Eq. (4) indicates that during synthesis, carbon monoxide (CO) is released during synthesis, thereby increasing the pressure in the working part of the chamber. Heating was conducted at a rate of 400°C/h. Pressure data were collected in 10°C increments.

Figure 1 illustrates a rise in the chamber pressure as temperature increases to 1520°C. This indicates the occurrence of the reaction outlined in Eq. (4), which involves the release of CO. It is obvious that the reaction begins at 1300°C. By examining the slope of the graph from 1300°C onward, we can determine that the maximum reaction rate for Eq. (4) occurs at temperatures between 1500 and 1520°C. The graph reveals that the synthesis reaction in a 3-g sample takes approximately 30 min. In our experiments, we exposed the samples for one hour at temperatures of 1350°C and 1450°C. As a result, the content of cerium dicarbide at a temperature of 1350°C did not exceed 10% of the sample, and at 1450°C, cerium dicarbide constituted slightly more than half of the sample mass. Referring to the Fe–C diagram, the maximum solubility of carbon in iron is 6.67%; at this concentration, the transition to the liquid phase occurs at 1247°C. Therefore, the synthesis of cerium dicarbide occurred in a liquid iron solution. This prevents future interaction of cerium dicarbide with water in the air when in a solid iron solution.

Cerium's high chemical activity is comparable to that of calcium. For example, calcium carbide is obtained from the reaction outlined in Eq. (1)

$$3C + CaO \rightarrow CaC_2 + CO. \tag{1}$$
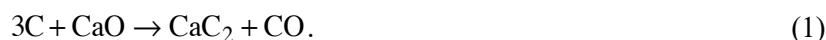
The reaction outlined in Eq. (1) occurs within the temperature range of 1600–1800°C when $C/CaO \geq 3$, yielding the reaction product CaC_2. However, when the C/CaO ratio is lower than 3 and the annealing temperature exceeds 1800°C, a two-stage mechanism is activated. This process involves the release of calcium vapor in stage 1 of Eq. (2) and the formation of calcium carbide in stage 2 of Eq. (3) [12]:

$$CaO + C \rightarrow Ca(g) + CO, \tag{2}$$

$$Ca(g) + 2C \rightarrow CaC_2. \tag{3}$$
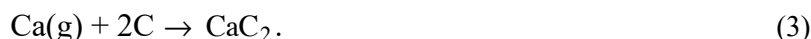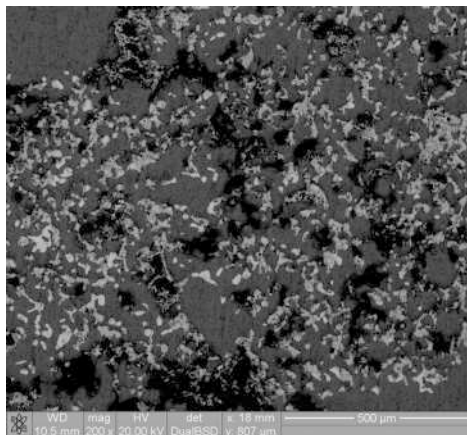
Fig. 2. Image of the microstructure of the Fe–Ce–C sample.

The chemical reaction of CeC_2 formation from CeO_2 and C is presented as follows:

$$CeO_2 + 4C \rightarrow CeC_2 + 2CO. \tag{4}$$

As mentioned above, the reaction outlined in Eq. (4) occurs in the temperature range of 1500–1520°C. This reaction, which happens in two states, requires a CeO_2/C weight ratio of 3.6.

$$2CeO_2 + C \rightarrow Ce_2O_3 + CO, \tag{5}$$

$$Ce_2O_3 + 7C \rightarrow 2CeC_2 + 3CO. \tag{6}$$

This scheme is a conclusion from experiments performed with changes in the synthesis temperature and charge compositions. For example, Figure 1 shows that up to a temperature of 1300°C, a reaction occurred with an increase in pressure in the working chamber of the furnace; when the charge with the stoichiometry of reaction of Eq. (1) was annealed at a temperature of 1200°C, the resulting sample consisted of a mixture of oxides Ce_2O_3, CeO_2, and C. When the ratio of CeO_2/C was changed to 7.2 by mass, the reaction result changed dramatically. It is probable that the reaction proceeds according to the following two-stage scheme:

$$Ce_2O_3 + 3C \rightarrow 2Ce(l) + 3CO, \tag{7}$$

$$Ce(l) + 2C \rightarrow CeC_2. \tag{8}$$

The mixture, at a heating rate of 10°C/min and held at a temperature of 1600°C for 60 min, lost 80% of its mass. It reacted with the Al_2O_3 crucible, resulting in the $CeAlO_3$ compound, as confirmed by X-ray phase analysis. At this temperature, the reaction to produce the $CeAlO_3$ compound could occur if Al_2O_3 reacted with cerium metal or with cerium vapor, given that the melting point of CeO_2 in the solid state is 2400°C.

The results of the microstructural analysis are presented in Fig. 2.

In Fig. 2, two phases can be distinguished: the light (presumably cerium dicarbide) and the dark (α-iron). Several pores also formed in the sample. Cerium dicarbide particles have an average size of 50 μm The EDAX analysis of these phases is presented in Fig. 3.

(a)

(b)

(c)
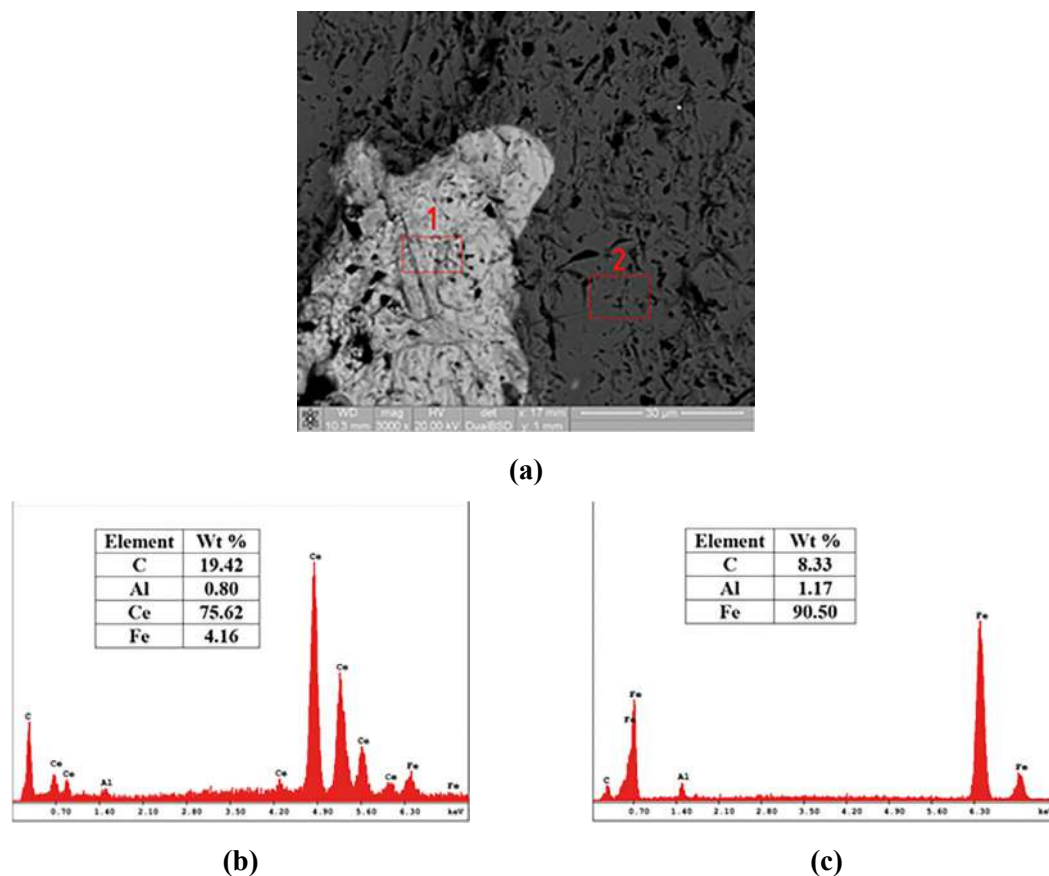
Fig. 3. Results of studying the elemental composition of the resulting sample: (a) snapshot of the structure with a magnification of × 3000; (b) spectrum of characteristic X-ray radiation and elemental composition obtained from zone *1*; (c) spectrum of characteristic X-ray radiation and elemental composition obtained from zone *2*.

Based on the results of elemental analysis, two phases can be distinguished in the resulting sample: white, presumably cerium dicarbide, and gray, an iron–carbon matrix. Aluminum impurities are noted, but their content in this alloy is inevitable towing to the use of a corundum crucible. Considering that no more than 0.2% cerium is added to steel, the content of aluminum in steel will be negligible. In addition, aluminum is an oxidizing agent. From the EDAX analysis, it is clear that the content of cerium and carbon in cerium dicarbide closely aligns with theoretical expectations, with iron constituting 4.16 wt.%.

The X-ray diffraction analysis results of the master alloy, obtained by sintering cerium dioxide, graphite, and ARMCO-iron, are presented in Fig. 4.

The phase composition and parameters of the crystal lattice of cerium dicarbide were determined by X-ray phase analysis. Figure 4 presents a typical powder X-ray diffraction pattern for CeC_2 products. All peaks in this spectrum correspond to the tetragonal phase CeC_2 (space group: I4/mmm(139)), which is consistent with standard literature data (PDF card number: 00-004-0711). X-ray phase analysis did not reveal the presence of any aluminum and iron compounds within cerium.

Experimental data, obtained by heating cerium and carbon in vacuum at temperatures above 1300°C, are consistent with the physical–theoretical thermodynamic model of the formation enthalpy of cerium carbide $\Delta H°$.

When constructing an empirical equation describing the thermodynamic properties of a compound, the so-called "effective charge" of the nucleus is usually introduced into the equation. This is the atomic number of
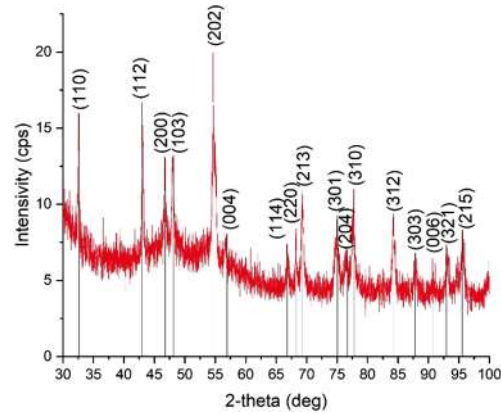
Fig. 4. Typical X-ray diffraction pattern of the CeC_2 compound taken from the surface oriented perpendicular to the pressing axis.

the element with an arbitrary correction. Thus, it is reduced to the enthalpy of particle interaction, without considering atomic–molecular bonds that determine the spatial arrangement of interacting particles and define crystalline systems with characteristic parameters.

Theory suggests that the formation enthalpy of $\Delta H(AB_x)$ is expressed as the specific enthalpy h:

$$h = -\frac{\Delta_f H}{\sum_{i=1}^{2} z},$$ (9)

where $\sum_{i=1}^{2} z = z(A) + xz(B)$ is the sum of the serial numbers of elements (nuclear charges) considering the stoichiometric composition of carbide. Specific enthalpy h is an effective quantity because it assumes that each nuclear charge has the same fraction of enthalpy.

The dependance of h on composition can be expressed as a linear equation:

$$h = a + Kx,$$ (10)

where K is the volumetric structural constant, encompassing linear structural constants and the coordination number of the crystal-forming substances.

When constructing a theoretical model, the entire field of the "property-composition" diagram is divided into regions of solid solutions, in which crystal-forming components are identified. In region 1 of solid solutions, the metal is always crystal-forming because by definition, its enthalpy of formation ΔH is 0. In other regions of solid solutions, any stable carbide for which the structure, composition, and enthalpy of formation are known can function as a crystal-forming component.

In any system, the dependance of the formation enthalpy of a substance $h - x$ starts from zero. This is the origin of region 1 of the solid solutions. Since each region of solid solutions possesses its own unique volumetric structural constant K, determined by the combination of structural constants of substances at the boundaries of the solid solution regions, the coordinates of the boundaries themselves are determined by jointly solving of the corresponding equations (2) for each region. The coefficient a is determined for each solid solution region by extrapolating the $h - x$ relationship to $x = 0$.

If we analyze similar dependence for heat capacity at constant pressure $1/C_p - x$ and specific entropy $\Delta S - x$, we can see that in the Ce–C system, there are two solid solution regions. The boundary between these

regions intersects with the composition of CeC_2. This is consistent with the fact that Ce and C have cubic lattices, whereas CeC_2 has a tetragonal lattice. Therefore, when constructing a theoretical model focusing on the formation enthalpy as the parameter under study, the diagram should also contain two solid solution regions with the same boundary.

When calculating specific entropy, it is vital to ensure consistency between the thermodynamic properties of individual substances and their compounds. Furthermore, the additivity of the entropy of substance formation should be considered.

The Gibbs energy DG is significant in chemical thermodynamics because the magnitude and sign of DG enable us to determine the state of the system, i.e., its position relative to equilibrium. By changing the intensity of system parameters, we gain the capability to control chemical processes.

In physical chemistry, the following equation is known:

$$\Delta G = \Delta H - T \Delta S. \tag{11}$$

Standard conditions for the formation of complex substances are illustrated in the following equation:

$$\Delta G^0 = \Delta H^0 - T_0 \Delta S^0. \tag{12}$$

The specific Gibbs energy $g = -\dfrac{\Delta_f G}{\sum\limits_{i=1}^{2} z}$, similar to the specific enthalpy h, forms two regions of solid solutions depending on the composition x. Given that $h(x)$, $\Delta S(x)$ within the region of solid solutions are linear functions of composition the dependence $G(x)$ should naturally exhibit a similar nature.

Building upon these insights and considering that the enthalpy of H formation is a state function, at any temperature other than 298 K, the standard change in the enthalpy of state (heat of reaction) can be calculated using the following equation:

$$\Delta H_T^o = \Delta H_{298}^o + \int\limits_{298}^{T} \Delta C_p \, dT. \tag{13}$$

When the above-described reaction initiates, two counteracting thermal processes occur at any point in the sample: heat release caused by an exothermic reaction and heat transfer resulting from the internal temperature gradient and radiation. If in any part of the sample the rate of exothermic heat release surpasses heat loss, then thermal energy starts to accumulate in that area. This causes a sharp temperature increase and triggers a self-sustaining reaction. Therefore, any parameter that increases the reaction rate at this stage (such as finer powder size) or reduces the rate of heat loss from the sample (such as low thermal conductivity of the material) causes thermal energy accumulation, which could initiate a self-sustaining reaction. This model can explain combustion during the synthesis of the Ce–C system.

The state diagram of the Ce–C system aligns with the following condensed phases of cerium carbides, for which Gibbs energy data for three cerium carbides is available [22]:

$$CeC: \; \Delta G = -116\,734 + 34.31T \; (915 - 940 \; (K)), \tag{14}$$

$$Ce_2C_3: \; \Delta G = -188\,280 - 14.64T \; (1\,071 - 1\,473 \; (K)), \tag{15}$$

$$CeC_2: \; \Delta G = -85\,228 - 26.98T \; (1\,071 - 2\,523 \; (K)). \tag{16}$$

Once carbon and cerium initiate a reaction via solid-state diffusion, the slope of the line indicating the sample temperature increases owing to the heat released from the exothermic reaction, as shown in Fig. 1. It is also important to note that the temperature difference between the furnace and the sample depends on the reaction rate. If the reaction rate is sufficiently enough that the rate of heat release within the sample surpasses the heat loss, then the sample temperature will increase exponentially. This significant temperature surge could potentially induce sample ignition.

Theoretical modeling enables us to interpret the experimental results obtained from examining the melting temperature of the Ce–C compound. These results are influenced by factors such as the heating rate, the size of the cerium and carbon particles, and the degree of preliminary compaction. For example, at high heating rates, the thickness of the CeC_2 layer produced by solid phase diffusion will be diminished once a specific temperature is attained. This reduction, in turn, will lead to a larger diffusion flux and temperature gradient. Therefore, increasing the heating rate will lead to a decrease in the ignition temperature. Obviously, reduced heat loss mirrors the effects of a high heating rate.

The effect of pretreatment on the melting temperature can be attributed to its impact on the thermal conductivity of the Ce–C system. As noted earlier, the higher the thermal conductivity, the higher the rate of heat loss, making melting more challenging. The upper and lower limits of preliminary compaction may be ascribed to the complex role that compaction density plays. A high density of the preliminary compaction of the Ce–C system components increases the contact points of the reactants, thereby accelerating the reaction rate and facilitating ignition. However, it also enhances thermal conductivity, which inhibits ignition. The volumetric heat capacity of the samples also increases as preliminary compression pressure rises, which usually affects the ignition temperature. A sample with a higher volumetric heat capacity demands more thermal energy to raise the sample temperature to the critical temperature for ignition, thereby preventing ignition.

CONCLUSION

This study analyzes a method for producing cerium dicarbide, which can be harnessed for the production of master alloys for steel and cast iron. The synthesis reaction involves sintering cerium dioxide, graphite, and ARMCO-iron in a specific percentage ratio by weight: 5.4% graphite, 19.5% CeO_2 cerium dioxide, and 75.1% ARMCO-iron. Laboratory research was performed in the temperature range from 1300°C to 1650°C. The optimal temperature range for synthesizing CeC_2 was found to be 1500–1520°C at a pressure of 10^{-1} mbar, with a cerium dioxide to carbon ratio of 3.6:1 by weight. With a twofold decrease in the amount of carbon, the reaction ceases to produce CeC_2 and instead results in the formation of gaseous Ce at a lower pressure. The master alloy does not undergo hydrolysis owing to the cerium carbide synthesis in the liquid phase of iron. Obtaining a master alloy based on cerium dicarbide by high-temperature heating in a resistive furnace enables the production of a material with reproducible properties. From a scaling perspective, sample mass virtually has no effect on the synthesis time.

REFERENCES

1. M. Laura and B. Bras, "Rare earth metal recycling," in: *Proceedings of the 2011 IEEE Intern. Symp. on Sustainable Systems and Technology* (2011), pp. 1–6.
2. N. Krishnamurthy, C. K. Gupta, and R. Earth, "Metals and alloys by electrolytic methods, mineral processing and extractive metallurgy review," *Int. J.,* **22** (4–6), 477–507 (2002); http://dx.doi.org/10.1080/08827500208547426.

3. D. K. Sahoo, H. Singh, and N. Krishnamurthy, "Current efficiency in electro-winning of lanthanum and cerium metals from molten chloride electrolytes," *Rare Met.,* **32**, 305–311 (2013); https://doi.org/10.1007/s12598-013-0060-y.

4. L. Yanqiang, W. Lijun, and G. Junbo, "Thermodynamic analysis of cerium inclusion formed in spring steel used in fastener of high-speed railway," *Chin. J. Nonferrous Met.,* **3**, 720–726 (2013).

5. W.-C. Jiao, H.-B. Li, H. Feng, Z.-H. Jiang, L.-F. Xia, S.-C. Zhang, H.-C. Zhu, and W. Wu, "Evolutions of micro- and macrostructure by cerium treatment in as-cast AISI M42 high-speed steel," *Metall. Mater. Trans. B,* **5** (2020); https://doi.org/10.1007/s11663-020-01912-x.

6. Gd. Zhao, Xm. Zang, Wm. Li, Z. Zhao, and Dj. Li, "Foundry C. Study on primary carbides precipitation in H13 tool steel regarding cooling rate during solidification," *China Foundry,* **17**, 235–244 (2020); https://doi.org/10.1007/s41230-020-9092-8.

7. Y. Huang, G. Cheng, M. Zhu, and W. Dai, "Effect of cerium on the behavior of primary carbides in cast H13 steels," *Metall. Mater. Trans. B,* **52b**, 700–713 (2021); https://doi.org/10.1007/s11663-020-02042-0.

8. Xy. Qiao, X. Han, Zj He, Z. Zhuang, X. Yang, and Fx. Mao, "Effect of cerium addition on microstructure and mechanical properties of as-cast high grade knives steel," *China Iron Steel Res. Inst. Group* (2022); https://doi.org/10.1007/ s42243-022-00798-0.

9. L. Xiao, Y. Ii-chun, Y. Lin, and G. Xue-zhong, "Effect of Ce on inclusions and impact property of 2Cr13 stainless steel," *J. Iron Steel Res. Int.,* **17**, 59–64 (2010); 10.1016/S1006-706X(10)60198-7.

10. Y.-W. Xu, S.-H. Song, and J.-W. Wang, "Effect of rare earth cerium on the creep properties of modified 9Cr-1Mo heat-resistant steel," *Mater. Lett.,* **161**, 616–619 (2015); https://doi.org/10.3390/met6080187.

11. S. Zhu, B. Yan, "Effects of Cerium on weld solidification crack sensitivity of 441 ferritic stainless steel," *Metals,* **9**, 372 (2019); https://doi.org/10.3390/met9030372.

12. C. Xin and X. Qian, "Reviews on technical routes for chemicals production from carbide acetylene," *Prog. Chem.,* **6**(01), 62–84 (1994). https://doi.org/10.3390/catal10080858.

13. C. Liu, R. I. Revilla, Z. Liu, D. Zhanga, X. Lia, and H. Terryn, "Effect of inclusions modified by rare earth elements (Ce, La) on localized marine corrosion in Q460NH weathering steel," *Corros. Sci.,* **129**, 82–90 (2017); http://dx.doi.org/10.1016/ j.corsci.2017.10.001.

14. H. Liu, P. Fua, H. Liu, Y. Cao, C. Sun, N. Du, and D. Li, "Effects of rare earth elements on microstructure evolution and mechanical properties of 718H pre-hardened mold steel," *J. Mater. Sci. Technol.,* **50**, 245–256 (2020); https://doi.org/10.1016/ j.jmst.2019.12.035.

15. L. Chen, X. Ma, L. Wang, and X. Ye, "Effect of rare earth element yttrium addition on microstructures and properties of a 21Cr-11Ni austenitic heat-resistant stainless steel," *Mater. Des.,* **32**(4), 2206–2212 (2010); https://doi:10.1016/j.matdes.2010.11.022.

16. Q. Ren, Z. Hu, L. Cheng, and L. Zhang, "Effect of rare earth elements on magnetic properties of non-oriented electrical steels," *J. Magn. Magn. Mater.,* **560**, 169624 (2022); https://doi.org/10.1016/j.jmmm.2022.169624.

17. Zhang Fei, Zhao Wei, Zhang Wengao, Liao Zexin, Xiang Xinhua, Gou Haojie, Li Zulai, Wei He, Wu Xing, and Shan Quan, "Microstructure, mechanical properties and wear resistance of rare earth doped WC/steel matrix composites: Experimental and calculations," *Ceram. Int.,* **49**, No. 2, 2638–2647 (2023); https://doi.org/10.1016/j.ceramint.2022.09.244.

18. Z. Adabavazeh, W. S. Hwang, and Y. H. Su, "Effect of adding cerium on microstructure and morphology of Ce-based inclusions formed in low-carbon steel," *Sci. Rep.,* **7**, 46503 (2017); https://doi.org/10.1038/srep46503.

19. L. N. Bartlett and B. R. Avila, "Grain refinement in lightweight advanced high-strength steel castings," *Int. J. Met.,* **10**, No. 4, 401–420 (2016); 10.1007/s40962-016-0048-0.

20. F. Haakonsen, J. K. Solberg, O. S. Klevan, and C. V. D. Eijk, "Grain refinement of austenitic manganese steels," *AISTech 2011 Proceedings,* **2**, 763–771 (2011).

21. E. T. Turkdogan, *Physical Chemistry of High Temperature Technology* [in Russian], Academic Press (1980).